

# Spatiotemporal scaling of turbulent photospheric line-of-sight magnetic field in the active region NOAA 11158

Jordan A. Guerra, Antti Pulkkinen, Vadim M. Uritsky, and Seiji Yashiro  
Catholic University of America and NASA Goddard Space Flight Center  
jordan.guerraaguilera@nasa.gov

Received \_\_\_\_\_; accepted \_\_\_\_\_

## ABSTRACT

We study structure and dynamics of the turbulent photospheric magnetic field in the active region NOAA 11158 by characterizing the spatial and temporal scaling properties of the line-of-sight (LOS) component. Using high-resolution high-cadence LOS magnetograms from SDO/HMI, we measured power-law exponents  $\alpha$  and  $\beta$  describing wavenumber- ( $k$ ) and frequency-domain ( $f$ ) Fourier power spectra, respectively, and investigated their evolution during the passage of the active region through the field of view of HMI. The (flaring) active region NOAA 11158 displays an average one-dimensional spatial power spectral density that follows approximately the power law  $k^{-3}$ ; a spectrum characteristic of a passive scalar field in a turbulent two-dimensional medium. In addition, we found that values of  $\alpha$  capture systematic changes in the configuration of the LOS photospheric magnetic field during flaring activity in the corona. Position-dependent values of the temporal scaling exponent  $\beta$  showed that, on average, the core of the active region scales with  $\beta > 3$  surrounded by a diffusive region with an approximately  $f^{-2}$ -type spectrum. Our results indicate that only a small fraction (6%) of the LOS photospheric magnetic flux displays  $\beta \approx \alpha$ , implying that the Taylor's frozen-in-flow turbulence hypothesis is typically not valid for the magnetic flux convected by turbulent photospheric flows. In consequence, both spatial and temporal variations of plasma and magnetic field must be included in a complete description of the turbulent evolution of the active region.

## 1. Introduction

Solar active regions (ARs) are the central building blocks in the path to understand the drivers of space weather. Major solar flares and coronal mass ejections (CME) originate from active regions, where the strong ( $\sim 10^3$  G) and complex magnetic field structures can accumulate sufficient free energy to power energetic eruptions. The high degree of complexity in terms of topology and spatial distribution present in the photospheric magnetic field appears to emerge from a turbulent photospheric plasma state (Abramenko (2005); Abramenko & Yurchyshyn (2010)). In this state, field emergence, fragmentation, and dissipation associated with turbulent flows lead to highly irregular spatiotemporal distribution of the magnetic field. Generally, we can view an AR as a system that takes the magnetic field and evolves it into an unstable non-potential configuration by non-linear shear and stress. For this system to return to a lower-energy state, the excess free energy must be released in a bursty event in the corona while electrical currents are dissipated and potential field configuration is restored (Shibata & Magara (2011)).

Non-linear dynamic processes, such as turbulence, are often studied using a description that involves statistical momenta of the turbulent field. For instance, in hydrodynamics (HD) and magnetohydrodynamics (MHD), the (kinetic and/or magnetic) energy injection, transfer, and dissipation process in turbulent flows are understood in terms of the scale-free behavior of their Fourier spectrum (Aschwanden (2011); Biskamp (1993)), which follows a power-law distribution. Kolmogorov-5/3 law is a classic example of this phenomena (Kolmogorov (1941)). In the case of the photospheric magnetic field, statistical parametric analyses have been performed with the aim of quantifying the complexity present in the field (see Abramenko (2005), McAteer et al. (2010)). However, only recently, when better and more accurate measurements of the photospheric magnetic field have become available, a

more coherent picture of the photospheric complexity has started to emerge (see Abramenko (2005)).

Previous studies of the photospheric magnetic field complexity in ARs can be divided into two categories: (1) analysis of the magnetic-field physical and statistical parameters such as the effective connected magnetic field strength (Georgoulis & Rust (2007); Georgoulis (2008)), the strong gradient length (Falconer et al. (2003, 2002)), or statistical moments of the spatial distribution of the field (Barnes & Leka (2008); Leka & Barnes (2003a,b)). (2) description of magnetic structures based on the transformations of the LOS magnetic field such as the spatial power scaling exponent (Fourier analysis; Abramenko (2005), Abramenko & Yurchyshyn (2010)) or the fractal dimension (wavelet analysis; McAteer et al. (2010)). For example, Georgoulis & Rust (2007) defined the AR effective connected magnetic field strength  $B_{eff}$  as a measure of magnetic field complexity. The  $B_{eff}$  parameter counts for the connectivity of individual photospheric magnetic flux concentrations, therefore its value depends on the spatial distribution of the flux concentrations. Values of  $B_{eff}$  were measured using LOS magnetograms averaged over 12 hours – a cadence too low in order to capture the transient phenomena of the magnetic concentrations regions, which encompass a wide range of temporal scales (Uritsky & Davila (2012); Uritsky et al. (2013)). Abramenko (2005) analyzed a sample of active regions using photospheric magnetic data from the Michelson Doppler Imager (MDI) instrument onboard SoHO and the Digital Magnetograph (DMG) located at the Big Bear Solar Observatory. The study focused on measuring the power-law scaling exponent of the spatial power spectral densities. Abramenko (2005) concluded that the derived exponents described the scale-free behavior of the magnetic field and served as indicators for differentiating between active regions that are prone to produce flaring activity and those that are flare-quiet.

A common approach in the studies mentioned above was to quantify the complexity present in the instantaneous spatial distribution of the photospheric field and then observe the subsequent time evolution of the spatial parameter. Consequently, spatial and temporal domain analyses have been conducted to most part in an independent fashion. A question that then naturally arises concerns the coupling between these two domains: is there a way to link the spatial and temporal variations? The first step to study the coupling is to verify the possible validity of Taylor's hypothesis of frozen-in-flow turbulence (Taylor (1938)) for the photospheric plasma. If the hypothesis is valid, determining the (temporal) spatial scaling (e.g. Abramenko et al. (2002)) is sufficient since the (spatial) temporal scaling is constrained to be identical. On the other hand, if the Taylor's hypothesis is not valid, both spatial and temporal scaling must be considered in the analysis in order to provide a complete picture of the state of the photospheric magnetic field and plasma. In the present report, we will demonstrate that the latter is indeed the case for the active region NOAA 11158.

In this paper, we extend previous studies of solar AR magnetic field complexity by addressing both spatial and temporal variability of the LOS photospheric magnetic field across wide ranges of scales. By constructing a more comprehensive picture of the turbulent spatiotemporal dynamics of the AR's photospheric field, we will provide new information that can help to better understand, for example, magnetic energy release signatures in the photosphere and coupling between photosphere and corona. In Section 2, we describe the analyzed set of LOS magnetograms and the active region to which they belong, NOAA 11158. Section 3 explains the data analysis and discusses the results. We explain the method of measuring the power-law exponents in two separated subsections: the spatial scaling analysis (Subsection 3.1) and the temporal scaling analysis (subsection 3.3), both based on the Fourier transforms of the LOS magnetic field. Our main results are reported and discussed in Subsections 3.2 and 3.4, while in Section 4 we draw conclusions and outline future work.

## 2. Data

### 2.1. Active Region NOAA 11158

The first X-class flare of the solar cycle 24 was generated by the active region NOAA 11158 on February 15, 2011 Schrijver et al. (2011). This active region containing two bipolar regions emerged on 2011 February 11 and was initially classified as a  $\beta$ -region according to the *McIntosh* classification (McIntosh (1990)). As the active region evolved, the two bipolar regions were seen colliding and then sliding along each other, forming a  $\beta\gamma$ -complex spot group Schrijver et al. (2011). At the time of the major flare, AR NOAA 11158 displayed three regions of intense magnetic field (see Figure 1): an eastern region of negative magnetic polarity, a western region of positive magnetic polarity, and a central region where a well defined *polarity inversion line* (PIL) separates the negative (north) from positive (south) polarities Bearegard et al. (2012). This active region has been studied widely (Wang et al. (2012); Schrijver et al. (2011); Bearegard et al. (2012)) because of the availability of data from many different instruments, and in particular high spatiotemporal resolution measurements from the *Solar Dynamics Observatory* (SDO). In addition to the X2.2-class flare, six M-class flares of different intensities were produced by AR NOAA 11158. Table 1 lists all seven flares indicating their classes, peak times, and rise times (i.e. time scale of the impulsive phase) according to the GOES X-ray 1 - 8 Å flux. For each flare, GOES X-ray 1 - 8 Å flux integrated over the corresponding rise time is reported in Table 1 as well.

### 2.2. Data set

We used a set of 4780 LOS magnetograms that spans 10 days, from February 10 to February 20, 2011, after which the active region disappears from the field of view in the

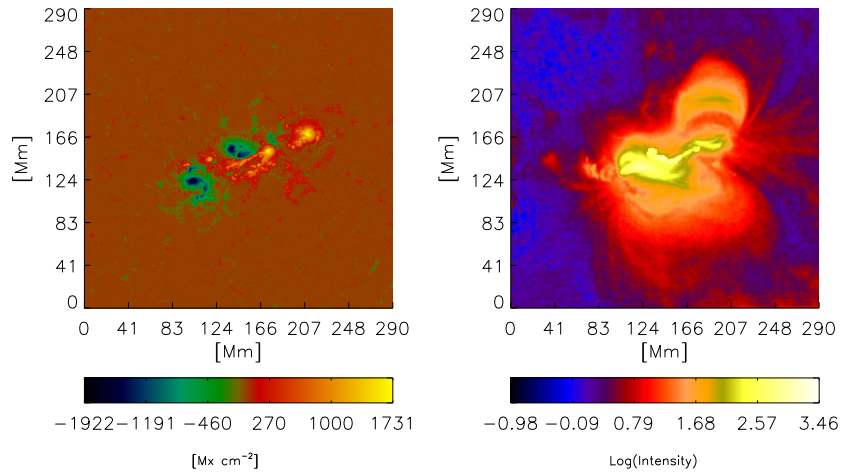


Fig. 1.— Spatial distribution of SDO/HMI line-of-sight magnetic field (left) and SDO/AIA 094 Å coronal emission (right) in the active region NOAA 11158 during the X2.2 flare of February 15, 2011 at 01:44 UT (onset time). The active region had a quadrupole line-of-sight magnetic configuration at the time of the flare.

western solar limb. Magnetograms of  $800 \times 800$  pixels displaying the active region were recorded by the *Heliospheric and Magnetic Imager* (HMI) (Scherrer et al. (2012)) on board the SDO satellite at spatial resolution of 0.5 arcsecond and a temporal resolution of 3 minutes.

The HMI instrument produces filtergrams measuring the Stokes parameters at different positions in the spectral line Fe I 617.3 nm. LOS magnetograms are calculated from the Stokes vector (Borrero et al. (2011)), producing imagery of the full disk at  $4096 \times 4096$  pixel with 0.5" per pixel and in near-real time cadence of 45 seconds. Magnetograms were corrected by using the IDL `drot_map` procedure on *SolarSoft* package. Each HMI magnetogram was remapped at the central meridian passage of the active region. Using the rigid option, the rotation rate was estimated to be 14.326 degree per day for all latitudes. At the central meridian position, the LOS component differs from the vertical component ( $B_z$ ) by a factor of

$\cos \theta$ , with  $\theta$  being the heliographic longitude at the center of the active region. Therefore, the LOS component was corrected by multiplying by  $[\cos(\theta)]^{-1}$  in order to evaluate the vertical component, assuming the field is radial (see Vemareddy et al. (2012) and references therein). Flaring activity in the active region was investigated also using the data from the *Atmospheric Imaging Assembly* (AIA) (Lemen et al. (2012)) aboard SDO. The AIA consists of 4 telescopes which measure coronal emission in 10 channels (EUV and UV) covering several Fe narrow-band measures, as well as the continuum for coalignment with other data (e.g. SDO/HMI, SoHO, TRACE). The AIA instrument enables high-resolution full-disk imaging of the corona and transition region, with a temperature range 0.06 to 20 MK, cadence of 12 seconds, and spatial resolution of 1.5". For the present work, we selected the 94 Å channel, corresponding to the Fe XVIII transition, which allows mapping of the flaring corona. In the Level 1.5 of the AIA data (Lemen et al. (2012)) maps were derotated, plate-scale adjusted, and shifted to place the center of the Sun in the middle of the detector. Finally, the coronal emission maps (Figure 1, right) were spatially and temporally coaligned with the HMI magnetograms (Figure 1, left), in order to correlate localized transient coronal features with the possible corresponding features in the photospheric magnetic field. We used GOES X-ray 1 - 8 Å flux of 1 minute cadence to identify the onset and the peak times of all the detected flares.

### 3. Results and Discussion

The scaling properties of the magnetic flux in active regions can be studied by measuring power laws of the power spectral density (PSD) as a function of either spatial wavenumber (Abramenko & Yurchyshyn (2010)) or temporal frequency. Power spectral density is calculated as the square of the absolute value of the Fourier spectrum, i.e.  $E(\nu)=|F(\nu)|^2$ , where  $\nu$  is either the Fourier frequency ( $f$ ) or wavenumber ( $k$ ). The Fourier spectrum is



obtained by using the Fast Fourier Transform method. Maximum and minimum measurable wavenumbers and frequencies for the spectrum are constrained by the image spatial size, spatial resolution, temporal resolution, and total length of the studied time series. When determining the possible scale invariance in the magnetic field variations, we focus on ranges of scales where the PSD follows approximately a power law. In subsections 3.1 and 3.3 we describe the spatial and temporal PSD analyses more in detail.

### 3.1. Spatial scaling

The instantaneous magnetic field distribution in each LOS magnetogram (see Figure 1, left) is a function of the horizontal and vertical positions,  $B_{LOS} = B(x, y)$ . Calculating the power spectrum of  $B(x, y)$  results in a two-dimensional PSD,  $E(k_x, k_y)$ , in which

$$k_{x,y} = \frac{n_{i,j}}{N_{x,y}\Delta_{x,y}} = \frac{n_{i,j}}{N_s\Delta_s}; \quad n_{i,j} = 1, 2, \dots, \frac{N_{x,y}}{2} - 1, \quad (1)$$

where in our case  $\Delta_x = \Delta_y = \Delta_s = 0.375$  Mm and  $N_x = N_y = N_s = 800$ .

One-dimensional (1D) PSD,  $E(k)$ , can be obtained from  $E(k_x, k_y)$  by integrating the latter over the angular direction. Here, we integrated the 2D PSD over quarter-circles of radius  $k = |k| = \sqrt{k_x^2 + k_y^2}$ . The meaning of the angle-integrated PSD is the spectral power of spatial magnetic field fluctuations associated with photospheric structures of the linear length  $l = k^{-1}$ . By applying the above transformation to each magnetogram in the set, we construct a time-varying PSD or dynamic spectrogram,  $E(k, t)$ .

Scale-invariant phenomena in non-linear dynamical systems are often characterized in terms of power-law distributions (see Aschwanden (2011), Chapter 1 for examples of

systems giving rise to power laws in physical sciences). Here we determine a power law in the wavenumber domain and follow the evolution of the exponent over time. That is

$$E(k, t) \sim k^{-\alpha(t)}, \quad (2)$$

The scaling exponent  $\alpha$  is defined as the slope in a log-log representation of the data (e.g. Abramenko (2005)). The exponent  $\alpha$  is measured within a range of  $k$  values that correspond to the estimated *inertial range* of photospheric turbulence (Biskamp (1993)). The inertial range involves scales which are smaller than the energy injection scale  $l_i$  and greater than the dissipation scale  $l_d$  (Abramenko et al. (2002); Biskamp & Welter (1989); Biskamp (1993)).

The time average of  $E(k, t)$  follows a power law in the wavenumber domain as well,  $\overline{E}(k) \sim k^{-\overline{\alpha}}$  in which  $\overline{\alpha}$  is the scaling exponent of the time-averaged spectrum. Figure 2 shows  $\overline{E}(k)$ . The best linear fit to this log-log graph can be obtained for the wavenumber range between  $k_{min}=0.05 \text{ Mm}^{-1}$  and  $k_{max}=0.5 \text{ Mm}^{-1}$  (vertical solid lines in Figure 2), or  $l \approx 2 - 20 \text{ Mm}$ . This inertial range of scales is defined in the high- $k$  limit by the presence of a "knee" in the PSD at  $k_{max}$ . At the low- $k$  limit, the value of  $k_{min}$  can vary. We found that this value does not affect significantly the measurement of  $\overline{\alpha}$ , giving us a flexibility of choosing the  $k_{min}$  value based on the best linear fit. In order to estimate the quality of the power-law fit, we calculate the  $R^2$ , the correlation coefficient between the data points in logarithmic scales and the predicted lineal model. Departures from  $R^2 = 1.0$  represent a less than ideally fitted model. We observed that the best-fit range of  $k$  in the temporally averaged spatial PSD, provides the best fit for measuring  $\alpha$  for also individual time steps. The inertial-range time-averaged scaling exponent,  $\overline{\alpha}$ , takes the value  $2.94 \pm 0.25$  with  $R^2 = 0.99$ . The uncertainty in the scaling exponent is obtained from the  $1-\sigma$  standard deviation of the linear fit in log-log space.

To verify the robustness of our implementation of the spectral analysis and to identify possible non-physical effects in the determined PSD, we tested our method on a set of synthetic images. We constructed the synthetic images in such a way they mimic the HMI data, i.e. they display fractals that have the same inertial-range scaling, dynamical range, and spatial size. For this purpose we have used the IDL `fractal_synth` routine which uses the Hurst exponent  $H$  (Hergarten (2002)) as input parameter. The Hurst exponent is related to  $\alpha$  as  $H = (\alpha - 2)/2$  for a two-dimensional fractal whose structure is continuous through the edges (the fractal forms a three-dimensional closed toroidal surface). In our computations we used  $H = 0.47$  which corresponds to  $\alpha = \bar{\alpha}=2.94$ . The set-averaged synthetic one-dimensional PSD is plotted in grey in Figure 2. Importantly, this curve shows that our implementation of the spectral analysis captures accurately the scaling through the entire range of generated synthetic data. The measured scaling exponent for the synthetic data is  $2.92 \pm 0.26$ . Differences between synthetic and physical PSD are clear for the high- and low-wavenumbers ends (Figure 2). The spectral power for the low- $k$  values is limited by the size ( $l \sim 50 - 80$  Mm) of the footpoints of the coronal arcades rooted in the active region (see Figure 1) and therefore the averaged PSD deviates from a straight line and becomes flat. On the other hand, for high wavenumbers the real PSD is seen to follow a different power-law scaling steeper than that in the synthetic data set.

The scaling  $k^{-3}$  is a characteristic of fluid flow velocity fluctuations in fully-developed two-dimensional Navier-Stokes turbulence (Biskamp (1993)). This feature suggests that the LOS component of the magnetic field in the active region is convected passively by turbulent horizontal flow field in the photosphere. Photospheric magnetic flux elements follow the velocity field which exhibits three distinct scales: granulation, mesogranulation, and supergranulation (Simon et al. (2001)). Flows in the granules (linear scale  $\sim 1$  Mm) are rather irregular and reflects the transport of energy by convection. Mesogranules (linear scale

$\sim 3 - 7$  Mm) are caused by collective interactions between adjacent granules. Mesogranules are often observed to drift to the edges of supergranules (linear size  $\sim 15 - 36$  Mm) which reflect a scale of convection deeper into the convection zone (Simon et al. (2001) and references therein). Mesogranules and supergranules therefore define the large-scale velocity field that passively convects the magnetic flux elements. In this picture, the  $k^{-3}$ -scaling observed in the inertial range of scales (2 - 20 Mm) reflects the convection of flux elements by the horizontal photospheric flow at the scale of mesogranulation. On the other hand, the presence of a kink in the power spectral density around  $l = 2$  Mm (Figure 2) is possibly associated with the change of photospheric flow dynamics from the mesogranular scale to granular scale. In this smaller range of scales the magnetic flux is expected to be dissipated as opposite sign flux elements annihilate each other.

### 3.2. Time evolution of $\alpha$

We also tracked the evolution of the scaling exponent  $\alpha$  as the active region moved across the solar disk, from the eastern to the western limb. During this time several flares were detected. Figure 3 displays the dynamics of the inertial-range exponent  $\alpha$  (top panel) and the coronal emission (bottom panel), as seen by the GOES X-ray 1 - 8 Å flux (blue) and the AIA 94 Å flux (red) integrated over the field of view. In both panels of Figure 3, vertical lines mark the onset time for the seven detected M- and X-class flares.

Based on the  $\alpha$  evolution, one can associate the emergence phase of the active region with the time interval 16 to 29 hours beginning from Feb. 9, 2011 23:59:19. After this time the total unsigned magnetic flux continues to grow, but  $\alpha(t)$  stayed within the range 2.8 to 3.4.

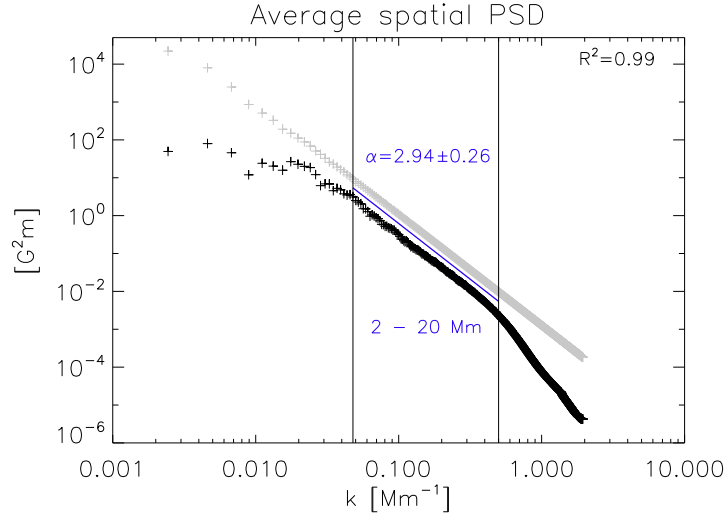


Fig. 2.— Power-law behavior of the average spatial power spectral density,  $\overline{E}(k)$ , as a function of wavenumber (black). The power-law exponent is determined within the inertial range of wavenumbers, marked by the vertical lines. The inertial range shows scaling with  $\overline{\alpha} = 2.94 \pm 0.25$ . The gray curve shows spatial spectral power density of synthetic data set with a measured exponent of 2.93. See text for details.  $R^2$  estimates the goodness of the linear fit and it is shown in the figure. The uncertainty of measure  $\pm 0.25$  represents the  $1\text{-}\sigma$  standard deviation.

At the beginning of the studied time interval, the inertial-range  $\alpha$  was slightly larger than the Kolmogorov value of  $5/3$  (marked with the horizontal dashed line in Figure 3). After about 18 hours, the exponent systematically increases until it reaches a value close to 3. Fluctuations of  $\alpha(t)$  around the mean value of  $\sim 2.9$  seen for the following 8 days are likely due to rearrangement of the existing photospheric flux as well as a newly-emerging magnetic flux. These slow  $\alpha$  variations could reach up to 10% of the mean value, and did not exhibit clear correlation with the flaring times. In agreement with Abramenko (2005), the flaring active region NOAA 11158 showed an inertial-range  $\alpha$  which was considerably greater than  $5/3$ .

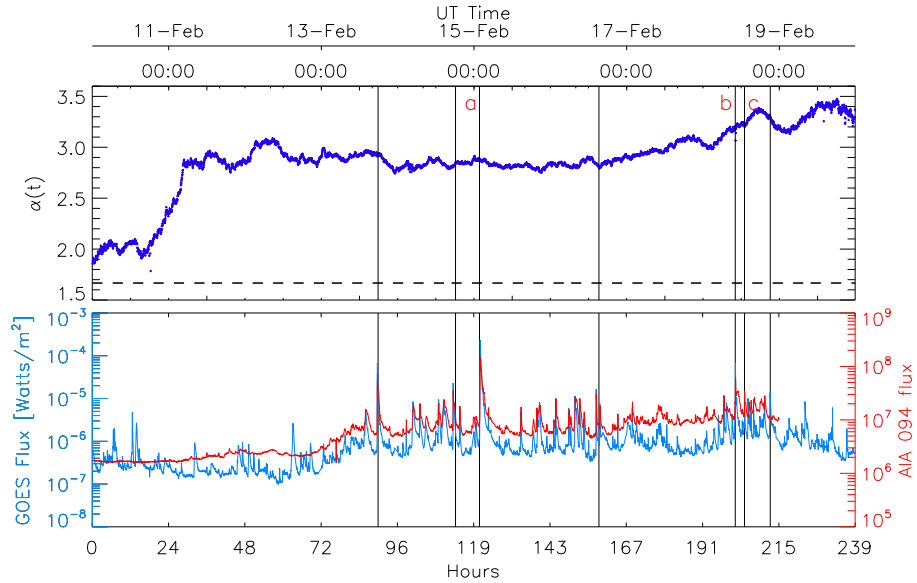


Fig. 3.— Time evolution of the scaling exponent  $\alpha$  (top panel) for the inertial range of spatial scales defined in the Figure 2, and the GOES X-ray and integrated AIA 094  $\text{\AA}$  fluxes (bottom panel), blue and red lines correspondingly. Vertical lines indicate flare onset times. The horizontal dashed line in the top panel marks the value of the Kolmogorov exponent  $5/3$ . Zero hours correspond to 02/09/2011 23:59:19.

In contrast to the long-term evolution discussed above, the short term evolution of this parameter over a course of several minutes does correlate with the coronal emissions. Figure 4 shows  $\alpha(t)$  for two ranges of scales of the normalized PSD  $E(k, t)/\bar{E}(k)$ , where the averaged spectra were computed over the 2-hours window shown in the figure. Measuring  $\alpha$  in the normalized spectra allows us to obtain values of the parameter that better captures changes in the spectral structure of the photospheric magnetic field. In addition to the inertial range (blue), we show  $\alpha(t)$  at small  $k$ -values which could be associated with the energy

injection range of the photospheric turbulence (Biskamp (1993); Abramenko & Yurchyshyn (2010)). Each panel in Figure 4 corresponds to a flare for which we detected association between  $\alpha(t)$  and GOES 1-8 Å and AIA 94 Å fluxes. Left panel corresponds to the X2.2-class flare observed on Feb 15 at 01:45 UT. Middle and right panels show a pair of M-class flares both of which occurred on Feb. 18. An M6.6-class flare with peak time 10:11 UT, and an M1.5-class flare which peaked at 13:03 UT. In all three cases we observed a systematic change of both time series of  $\alpha(t)$  around the flare time. In Figure 4 it is observed these changes are present in the magnetic field in two forms: transient or permanent (Vemareddy et al. (2012)). Transient changes are associated to contamination of the magnetic data (artifacts) (Vemareddy et al. (2012)), which are predominant during the flare impulsive phase and they display times scales comparable to that phase (see Table 1). Persistent changes, which are not related to artifacts, can be evident by taking the average value of  $\alpha(t)$  over 1 hour, before and after the flare. We found that this average value changes after the eruption suggesting that the state of the post-flare photospheric magnetic field is different from the state of the pre-flare photospheric magnetic field. This type of permanent changes are evident in the net signed magnetic flux density times series when the X2.2-class flare occurs (Figure 5). For this case, a rapid increase of the total flux density is observed.

Systematic changes in  $\alpha(t)$  around flaring times can be interpreted as a photospheric response to the reconnection taking place in the corona. This scenario suggests the possibility of a back-reaction from the corona to the photosphere soon after the flare takes place. The idea that the photosphere might respond to the magnetic reconnection in the corona has been previously proposed and discussed. Several authors have reported observations of correlated changes in the photospheric magnetic field, both in the full vector field and LOS component (see e.g. Wang et al. (2012), Li et al. (2011), Liu et al. (2005), Petrie & Sudol (2010), Vemareddy et al. (2012)). Furthermore, we showed that spectral scaling parameters, such as

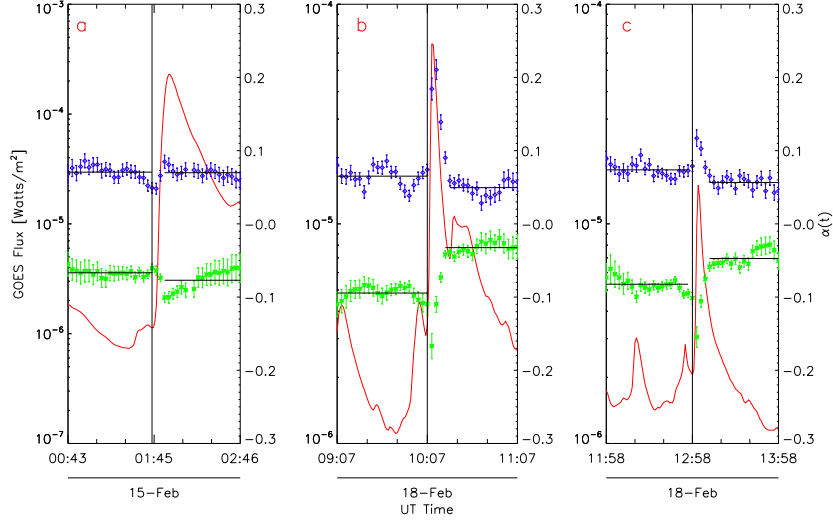


Fig. 4.— Short term temporal evolution of spatial scaling exponent  $\alpha$  around three flares: the X2.2-class flare (panel a) on Feb. 15, and two M-class flares on Feb. 18 (panel b and c, respectively). The exponents were measured for the normalized PSD and shifted vertically ( $\alpha(t)+0.07$  for blue lines,  $\alpha(t)-0.07$  for green lines) for better visualization. The size of the time window of each panel is  $40 \times \Delta t (3 \text{ min}) = 2 \text{ hours}$ . Panels a, b, and c correspond to Labels a, b, c in Figure 3.

$\alpha$ , calculated from photospheric magnetic data with sufficient spatiotemporal resolution can be used to study the photosphere-corona coupling.

### 3.3. Temporal scaling

Our temporal scaling analysis focuses on time series of signed magnetic flux density. First, we illustrate the method by analyzing time series of net magnetic flux density. Second, the method is applied to a set of subfields, with sizes comparable with the typical size of a



Table 1: Integrated GOES X-rays flux,  $F_{GOES}$  and rise time  $\Delta t$  for all 7 detected flares of class M and X emitted from the active region NOAA 11158. The rise time corresponds to the difference between the peak and the onset time, according to GOES X-rays 1-8 Å flux time series. The  $F_{GOES}$  flux is obtained by integrating the GOES X-ray 1 - 8 Å flux over  $\Delta t$  for each flare. This flux corresponds to that released during the flare impulsive phase.

GOES class	Peak time [UT Time]	$F_{GOES}$ [ $J/m^2$ ]	$\Delta t$ [min]
M6.6	Feb. 13, 17:38	$1.53 \times 10^{-2}$	7
M2.2	Feb. 14, 17:26	$2.27 \times 10^{-3}$	3
X2.2	Feb. 15, 01:56	$5.19 \times 10^{-2}$	10
M1.1	Feb. 16, 14:25	$1.47 \times 10^{-3}$	4
M6.6	Feb. 18, 10:11	$3.49 \times 10^{-3}$	3
M1.5	Feb. 18, 13:03	$1.29 \times 10^{-3}$	3
M1.3	Feb. 18, 21:04	$3.22 \times 10^{-3}$	9

granulation cell.

We constructed the time series of the net signed magnetic flux density (Figure 5) by summing, at each time  $t$ , the contributions from all magnetogram pixels,  $B(t) = \sum_{i,j} B_{LOS}(x_i, y_j, t)$ . The obtained time series was analyzed by using the FFT algorithm with a Hanning-type window (Press et al. (1992)). Similarly to the spatial analysis, the frequencies are defined as

$$f = \frac{i}{w\Delta_t}; \quad i = 1, 2, \dots, \frac{w}{2} - 1, \quad (3)$$

where  $\Delta_t = 3$  min is the time resolution and  $w$  is the window length. The maximum and minimum measurable frequencies are  $f_{max} = \frac{1}{2\Delta_t}$  and  $f_{min} = f_{max}/w$ , respectively. We applied this procedure to each point of  $B(t)$  in order to construct the dynamic spectrogram,  $E(f, t)$ , the temporal counterpart of  $E(k, t)$  defined in subsection 3.1.

The power-law decay of the Fourier power density was analyzed using the fit,

$$E(f, t) \propto f^{-\beta(t)}, \quad (4)$$

where  $\beta$  is the temporal scaling exponent, which evolves in time. This exponent characterizes non-stationary temporal autocorrelations in the time series. When determining  $\beta$  we used a window of 512 data points centered at each time point, or  $w = 1536$  min. This procedure was used to verify the applicability of Taylor's hypothesis in different regions (Figure 7). Figure 6 displays the time-averaged temporal PSD as a function of frequency,  $\overline{E}(f)$ . We measured the time-averaged scaling exponent  $\overline{\beta}$  of this spectrum following the same procedure as the one described in subsection 3.1. The range of frequencies which provided the best fit ( $R^2 = 0.97$ ) is  $4.3 \times 10^{-5} - 1.0 \times 10^{-3} \text{ s}^{-1}$  or 17 to 380 min. Within this range of frequencies,  $\overline{\beta} = 1.63 \pm 0.32$

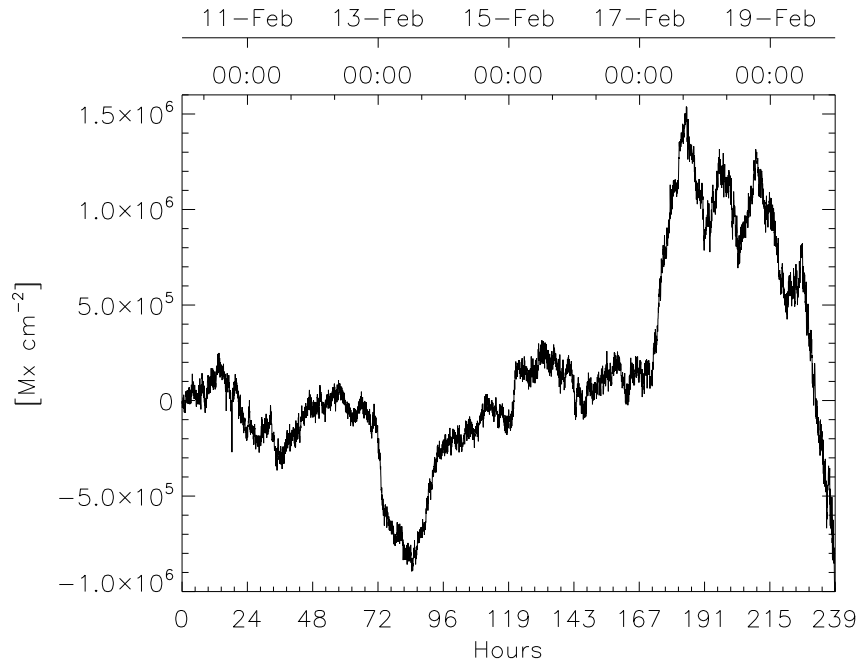


Fig. 5.— Time series of the net signed magnetic flux density ( $B(t)$ ) in the active region NOAA 11158. The apparent unbalance of  $B(t)$  could be caused by the limited field of view, the projection effects, or the asymmetric fragmentation leading to an underresolved magnetic flux of one polarity (Lamb et al. (2008)).

which reveals that the time evolution of total signed magnetic flux density may follow approximately a Kolmogorovian spectrum,  $f^{-5/3}$  (Kolmogorov (1941)).

Statistical characteristics of stochastic processes are conveniently described in terms of the specific value of  $\beta$ , the power-law scaling exponent. For instance,  $\beta = 0$  corresponds to a white noise process,  $\beta = 2$  to a Classical Brownian Motion, and any other value corresponds to a fractional Brownian motion, fBm, (Mandelbrot (1982); Hergarten (2002)). Furthermore, power-law spectral density scaling with  $\beta < 2$  is an indication of anti-persistence in  $B(t)$  following fBm, i.e. the time series reverts its tendency more often than a classical random

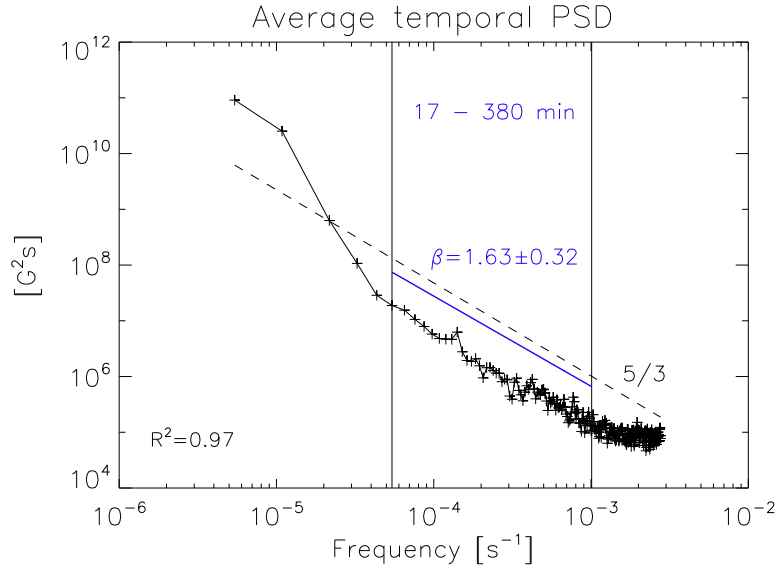


Fig. 6.— Double-logarithmic plot of the averaged temporal power spectral density. Vertical lines mark the range for which we carry out the power-law fit and measure the exponent  $\beta$ . Photospheric LOS magnetic structures with lifetimes (or periods) between 17 and 380 min present an approximate Kolmogorovian scaling in frequency ( $f^{-5/3}$ , black dashed curve).

walk, since the increments are negatively correlated. In other words, if  $B(t)$  was increasing in a previous period, it is more likely that it will decrease in the next period and vice versa. This observed anti-persistent behavior may represent a balance between the supplied and dissipated photospheric magnetic flux involving a negative feedback. A negative feedback takes place when the output of a non-linear system is used to "control" the input in such a way that stability can be achieved and fluctuations reduced. Based on measured  $\beta$  value, we can speculate that the photosphere behaves locally as a self-regulating system: the rate at which the flux is injected into (input) the photosphere is influenced by the rate at which the flux is dissipated (output) in order to maintain steady level of total magnetic flux. We also point out that balance between the injected and the dissipated energy is a characteristic of stationary turbulence (Biskamp (1993)).

In particular, we believe the negative feedback that is inferred from the scaling of the power spectrum is a manifestation of steady turbulence necessary for maintaining the steady state of the solar global magnetic network (Simon et al. (2001)). Active regions are known to be embedded in the global photospheric network of magnetic elements. It has been reported that this network exists in a statically steady state with a total unsigned flux of  $2 - 3 \times 10^{23}$  Mx over the whole solar surface (Simon et al. (2001)). Such a steady state can be maintained if magnetic flux is supplied at a rate of approximately  $7 \times 10^{22}$  Mx day<sup>-1</sup>. According to (Simon et al. (2001)), flux elements with intensities greater than  $10^{18}$  Mx can be convected by supergranular flows towards the edges of the supergranules; there elements eventually meet with an opposite sign element and cancel out each other (annihilation). Therefore, in order to maintain the total flux intensity constant, flux elements must be injected into the photosphere at a rate that is comparable to lifetimes of the already existing flux elements. The spectrum in Fig. 6 suggests that this process is controlled by fully-developed fluid turbulence.

### **3.4. Studying the validity of Taylor’s Hypothesis for the Photospheric Turbulence**

It is often a challenge to measure both spatial and temporal fluctuations in turbulent flows with sufficient level of accuracy. For instance, the usage of multiple probes in plasma experiments can introduce a distortion in the flows that are observed. Less intrusive measurement techniques, such as a laser diagnostic, can provide an adequate spatial resolution, but tend to have limited temporal resolution. To address this issue, Taylor (1938) proposed a way to relate the spatial and temporal characteristics of turbulence. If we study the dynamics of turbulence in terms of the Fourier representation, the temporal fluctuations

$f$  of a fixed point in space by the passing of a Fourier mode with frequency  $\omega$  and isotropic wavevector  $k$  is (Moin (2009))

$$2\pi f = \omega + \vec{v} \cdot (2\pi\vec{k}), \quad (5)$$

where  $\vec{v}$  is the bulk velocity and  $\vec{k}$  is in the units of  $\text{m}^{-1}$ . We can represent the velocity field of the fluid as  $\vec{v} = \vec{U} + \vec{u}'$ , where the  $\vec{U}$  is the average flow speed and  $\vec{u}'$  represents the fluctuations due to turbulence. Taylor's hypothesis states that, in the presence of isotropic turbulence for which  $u' \ll U$  (where  $u' = |\vec{u}'|$  and  $U = |\vec{U}|$ ),  $\omega \approx 0$ . The intrinsic temporal variation of the flow can be ignored. Thus, Equation (5) becomes

$$f \approx Uk. \quad (6)$$

Therefore the temporal response at a fixed point expresses the mode  $k$ , which is convected through the point at the average speed of the flow. As is seen from Equation (6), in this way it is possible to infer the temporal behavior of turbulence from its spatial behavior and vice versa. In terms of power-law scaling, if  $E(k) \sim k^{-\alpha}$  is the scaling in the spatial domain, we expect an identical power law in the frequency domain, that is, using Equation (6)  $E(k = f/U) \sim (f/U)^{-\alpha}$  or  $E(f) \sim f^{-\alpha}$ . In other words, we expect  $\beta = \alpha$  if the Taylor's hypothesis holds.

In Subsection 3.1, we found that the time-averaged 1D spatial PSD for  $B_{LOS}$  follows approximately the power law  $\overline{E}(k) \propto k^{-3}$  for an inertial range of scales of 0.05 - 0.50  $\text{Mm}^{-1}$ . In Subsection 3.3, we measured the average temporal scaling for the time series of integrated flux density which followed approximately the power law  $\overline{E}(f) \propto f^{-5/3}$ . Because of the averaging process, the latter scaling law does not contain any spatial information. Since the

two power-law exponents do not match, it is clear that the Taylor’s assumption does not hold on average. However, this assumption can still be valid at particular locations and/or during specific time intervals. This sections aims at testing this possibility. To fulfill this goal, we measured position-dependent values of  $\beta$  to construct a  $\beta$  map. Using this map, we have searched for regions where  $\alpha \approx \beta$  and therefore the Taylor hypothesis of frozen-in-flow turbulence is approximately valid.

In order to construct the map of  $\beta$ -values, we divided the studied field of view into non-overlapping subregions of  $8 \times 8$  pixels, and averaged the signed flux density over these subregions for each time step. The resulting time series were analyzed as described in section 3.3, using FFT with  $w=1536$  min and the sliding window step of 150 min.

In the solar photosphere, there are several relevant wave speeds such as: the sound speed ( $c_s = (\gamma p_0 / \rho_0)^{0.5}$ ), the Alfvén speed ( $v_A = B_0^2 / \sqrt{\mu \rho_0}$ ), and the slow magnetoacoustic speed ( $c_t = c_s v_A / (c_s^2 + v_A^2)^{0.5}$ ) (Murdin (2003)). Each of these speeds represents a different physical mechanism of transferring energy and information. In the above definitions,  $\rho_0$ ,  $p_0$ , and  $B_0$  are characteristic values of plasma density, pressure, and magnetic field strength in the photosphere, while  $\gamma$  and  $\mu$  are the ratio of specific heat of the plasma and the magnetic permeability, correspondingly. For typical photospheric conditions  $c_s = 11 \text{ km s}^{-1}$ ,  $v_A = 12 \text{ km s}^{-1}$ , and  $c_t = 8.1 \text{ km s}^{-1}$  (Murdin (2003)). Another relevant energy transfer process is plasma convection in the photospheric plane. The typical horizontal component of the convection velocity,  $v_{hc}$ , lies in the range of  $0.45 - 0.50 \text{ km s}^{-1}$  (Shine et al. (2000)). In order to obtain the best power-law fit, we have chosen the upper limit of this range ( $0.50 \text{ km s}^{-1}$ ) as a proxy to  $v_{hc}$ . Also, since values of  $c_s$ ,  $v_A$ , and  $c_t$  are comparable, we have represented them all by a single value  $v_{MHD}$  corresponding to the average of the three speeds,  $10.4 \text{ km}$

$s^{-1}$ . Substituting the values of  $v_{hc}$  and  $v_{MHD}$  for  $U$  in Equation (6), and using the inertial range  $k = 0.05 - 0.35 \text{ Mm}^{-1}$  we calculated the corresponding ranges of frequencies for measuring the scaling exponent  $\beta$ :

- Range 1:  $4.05 \times 10^{-4} - 1.5 \times 10^{-3} \text{ s}^{-1}$  (periods: 4 - 41 min) for  $v_{MHD}$ ,
- Range 2:  $2.50 \times 10^{-5} - 2.50 \times 10^{-4} \text{ s}^{-1}$  (periods: 66 - 660 min) for  $v_{hc}$ .

By using these two ranges, we have divided the temporal PSD into two parts, each one described by a different scaling exponent. The low frequency part of the PSD corresponds to the mapping of the inertial range due to the convection speed and the high-frequency part that encompasses the MHD wave speed range. In addition to these ranges, we also tried to measure exponent  $\beta$  over an empirical range providing the best power-law fit to the temporal PSD.

Figure 7 displays the map of temporal scaling exponents  $\bar{\beta}$  measured for the time-averaged temporal PSD (top panel), and time series  $\beta(t)$  of instantaneous exponent values for sub-regions  $a$  and  $b$  (bottom panel). These values of  $\bar{\beta}$  and  $\beta(t)$  were calculated using the range 2 defined above, corresponding to the horizontal convection speed. It can be seen that different areas in the field of view have different values of  $\bar{\beta}$ : 1) Outside of the active region, the magnetic fluctuations represent a combination of two types of stochastic behavior: flicker-type noise ( $f^{-1}$ , blue) and a Brownian noise ( $f^{-2}$ , green). At the boundary of the active region  $\bar{\beta} \approx 2.0 - 2.3$ , while in the core of the active region,  $\bar{\beta} > 3$ . The value  $\bar{\alpha} = 2.94$ , the scaling exponent of the time-averaged spatial PSD (Subsection 3.1), is shown on the color bar of Figure 7 for comparison. Photospheric regions where the scaling exponents  $\bar{\alpha}$  and  $\bar{\beta}$  are those where Taylor's hypothesis is approximately valid. Note that time-dependent values  $\beta(t)$  at locations  $a$  and  $b$  can deviate considerably from their average values  $\bar{\beta} \approx 3$  and



$\bar{\beta} \approx 2.5$ , respectively. Thus, even when Taylor’s hypothesis locally holds on average, as is the case for region  $a$ , there is a considerable variation in  $\beta$  over time.

Similar maps of  $\bar{\beta}$ -values were obtained for the range of frequencies calculated using the MHD wave speed (range 1) as well as the empirical range yielding the best fit. The  $\bar{\beta}$  values of these ranges varied between 0.39 and 2.35. No location within the field of view showing  $\bar{\beta} \approx \bar{\alpha}$  was identified for these ranges.

In Figure 7, the area of the photosphere characterized by  $\bar{\beta} \approx \bar{\alpha} = 2.94 \pm 0.25$  (see Figure 2) is only about 6% of the field of view. This indicates that typically spatial and temporal scaling behavior of the photospheric plasma cannot be linked by simply using Taylor’s approximation. Therefore, in order to obtain a full description of this system, an independent information about spatial and temporal aspects of its behavior needs to be considered.

#### 4. Conclusions

We have investigated the turbulent state of the line-of-sight photospheric magnetic field by characterizing its Fourier spectral density, both in the spatial and temporal domains. Using power-law spectral exponents  $\alpha$  (spatial) and  $\beta$  (temporal), we studied the photospheric plasma dynamics and its possible implications for the photosphere-corona coupling. In this investigation we used high-spatial-resolution high-cadence LOS magnetograms and maps of coronal emission from SDO/HMI and SDO/AIA, correspondingly. The utilized data represent the active region NOAA 11158.

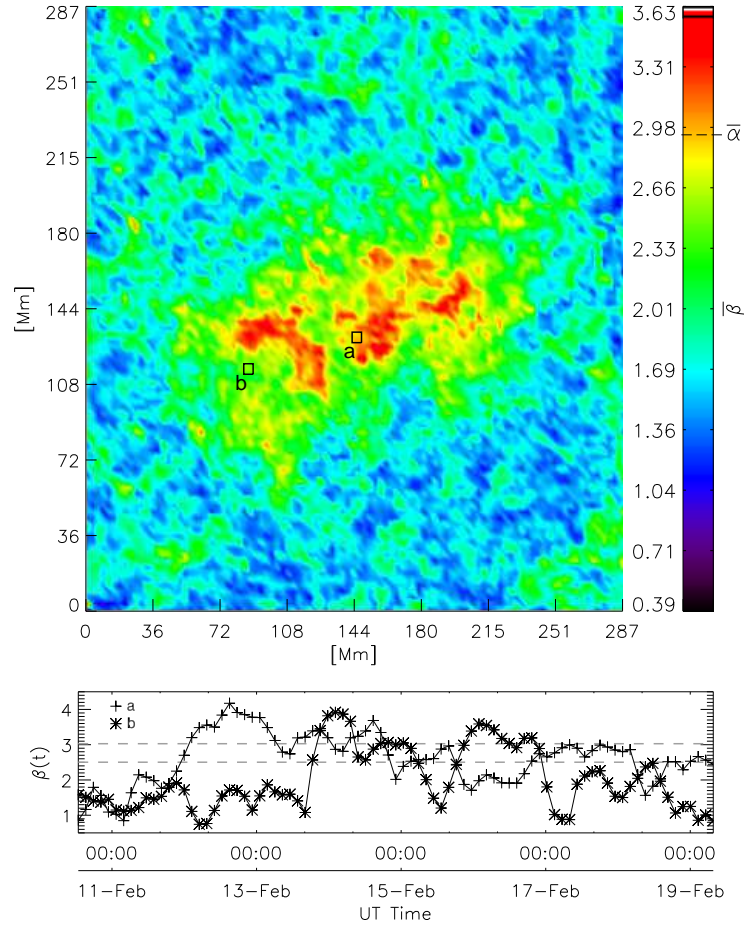


Fig. 7.— *Top*: Spatial distribution of values of the averaged temporal scaling exponent,  $\bar{\beta}$  measured in the range of frequencies  $2.5 \times 10^{-5} - 2.5 \times 10^{-4} \text{ s}^{-1}$ . This range corresponds to inertial range of  $k$  scales  $0.05 - 0.5 \text{ Mm}^{-1}$  mapped by using the nominal horizontal convection speed of the photospheric flow of  $500 \text{ m/s}$ . *Bottom*: Time series of  $\beta$  on the sub-regions  $a$  and  $b$  indicated in the top panel.

We determined the spatiotemporal scaling in two stages. First, the scaling was studied by measuring the spatial scaling exponent  $\alpha$  of the LOS power spectral density. In the second stage we carried out the temporal analysis, in which we determined the temporal scaling of

the total LOS magnetic field.

Time-averaged and time-dependent values of the spatial scaling exponent were measured for the turbulence inertial range of scales, that were determined here to be scales with linear sizes  $l = k^{-1} \approx 2 - 20$  Mm. The average power spectrum,  $\overline{E}(k) \sim k^{-\overline{\alpha}}$ , provided scaling exponent  $\overline{\alpha} \approx 3$ . In addition, the time evolution of the exponent,  $\alpha(t)$ , showed that the flaring active region photospheric field scaled as  $\alpha(t) > 5/3$  in agreement with Abramenko & Yurchyshyn (2010). The power law  $k^{-3}$  corresponds to the power spectrum of a two-dimensional turbulent hydrodynamical flow. This observation suggests that the LOS photospheric magnetic field may behave as a passive scalar that is moved in the photospheric plane by the turbulent horizontal mesogranular plasma flows.

Temporal spectral analysis of the data showed that the time series of the total signed LOS magnetic flux density displays a power-law spectrum which can be approximated by the Kolmogorov exponent  $E(f) \propto f^{-5/3}$  for an inertial range of temporal scales from several minutes to several days. In general, time series presenting a power-law spectra with  $\beta \neq 2$  are described in terms of the fBm model. In particular, for  $\beta \approx 5/3$  a fBm time series displays an anti-persistent behavior with weakly-anticorrelated increments. In the context of photospheric magnetic field evolution this fBm behavior could be an indication of a system seeking for a balance between the injection and dissipation of photospheric magnetic flux. We believe this balance is a signature of fully-developed turbulence that controls the photospheric magnetic flux dynamics and it is present in order to maintain the statistically steady state of the global photospheric magnetic network (Simon et al. (2001)).

Position-dependent average values of the temporal scaling exponent  $\overline{\beta}$  indicated that

regions with high average magnetic flux densities are typically associated with a higher spectral slopes. Exponents  $\bar{\beta}$  were measured for a range of frequencies corresponding to the spatial inertial range. We found that only about 6 % of the studied image area satisfies the condition  $\bar{\beta} \approx \bar{\alpha}$ . This implies that Taylor’s frozen-in-flow turbulence hypothesis is invalid for 94% of the field of view, including most of the active region. Consequently, a linear mapping between spatial and temporal behavior using the Taylor’s hypothesis seems impossible, and a full spatiotemporal characterization of the photospheric magnetic field is required for a complete description of the turbulent dynamics of the system. We have carried out the first initial steps towards such spatiotemporal characterization in this work.

The short-term evolution (minutes to a few hours) of the spatial scaling exponent  $\alpha$  captures systematic changes in the spatial distribution of LOS photospheric magnetic field associated with flaring activity. The flare-related changes manifest themselves in both transient (9 - 12 min) and persistent ( $\sim 1$  hour or longer) variations of  $\alpha(t)$  at the time of the flare and immediately afterwards, respectively. The transient variations in  $\alpha(t)$  are most likely associated with artifacts in the magnetic field data, while the persistent changes suggest a change in the state of the photospheric field. The active region NOAA 11158 produced 6 M-class flares during its passage through the solar disk. We detected such systematic changes for two of these flares, in addition to the X-class flare. Although our results support the idea of a back reaction from the corona to the photosphere right after a flare occurs, careful analyses of a larger data set are required to confirm what types of flares are capable of influencing the post-flare state of the photospheric magnetic field.

Careful spatiotemporal analysis of high-resolution photospheric and coronal images such as the one conducted in this study can improve our understating of the physics of the active

regions and the links between the photosphere and the corona during flaring activity. Furthermore, photospheric parameters such as the scaling exponents  $\alpha$  and  $\beta$  may also contain advance information about the flaring activity in the solar corona. We will expand our studies initiated in this paper by inclusion of new active regions into analyses and by using full vector photospheric magnetic field data. Our ultimate goal is to better understand the physical properties of faring active regions and to seek for new precursors for pending major solar eruptions.

*Acknowledgements:* SDO/HMI team. This work was done under CEPHEUS cooperative agreement between Catholic University of America and NASA Goddard Space Flight Center. We thank Dr Karin Muglach for useful discussions.

## REFERENCES

- Abramenko, V., & Yurchyshyn, V. 2010, *ApJ*, 720, 717
- Abramenko, V. I. 2005, *ApJ*, 629, 1141
- Abramenko, V. I., Yurchyshyn, V. B., Wang, H., Spirock, T. J., & Goode, P. R. 2002, *ApJ*, 577, 487
- Aschwanden, M. J. 2011, *Self-Organized Criticality in Astrophysics*
- Barnes, G., & Leka, K. D. 2008, *ApJ*, 688, L107
- Beauregard, L., Verma, M., & Denker, C. 2012, *Astronomische Nachrichten*, 333, 125
- Biskamp, D. 1993, *Nonlinear magnetohydrodynamics*
- Biskamp, D., & Welter, H. 1989, *Physics of Fluids B*, 1, 1964
- Borrero, J., Tomczyk, S., Kubo, M., et al. 2011, *Solar Physics*, 273, 267
- Falconer, D. A., Moore, R. L., & Gary, G. A. 2002, *ApJ*, 569, 1016
- . 2003, *Journal of Geophysical Research (Space Physics)*, 108, 1380
- Georgoulis, M. K. 2008, *Geophys. Res. Lett.*, 35, 6
- Georgoulis, M. K., & Rust, D. M. 2007, *ApJ*, 661, L109
- Hergarten, S. 2002, *Self-Organized Criticality in Earth Systems*
- Kolmogorov, A. 1941, *Akademiia Nauk SSSR Doklady*, 30, 301
- Lamb, D. A., DeForest, C. E., Hagenaar, H. J., Parnell, C. E., & Welsch, B. T. 2008, *ApJ*, 674, 520

- Leka, K. D., & Barnes, G. 2003a, *ApJ*, 595, 1277
- . 2003b, *ApJ*, 595, 1296
- Lemen, J., Title, A., Akin, D., et al. 2012, *Solar Physics*, 275, 17
- Li, Y., Jing, J., Fan, Y., & Wang, H. 2011, *ApJ*, 727, L19
- Liu, C., Deng, N., Liu, Y., et al. 2005, *ApJ*, 622, 722
- Mandelbrot, B. B. 1982, *The Fractal Geometry of Nature*
- McAteer, R. T. J., Gallagher, P. T., & Conlon, P. A. 2010, *Advances in Space Research*, 45, 1067
- McIntosh, P. 1990, *Solar Physics*, 125, 251
- Moin, P. 2009, *Journal of Fluid Mechanics*, 640, 1
- Murdin, P. 2003, *Encyclopedia of Astronomy and Astrophysics*
- Petrie, G. J. D., & Sudol, J. J. 2010, *ApJ*, 724, 1218
- Press, W. H., Teukolsky, S. A., Vetterling, W. T., & Flannery, B. P. 1992, *Numerical recipes in FORTRAN. The art of scientific computing*
- Scherrer, P., Schou, J., Bush, R., et al. 2012, *Solar Physics*, 275, 207
- Schrijver, C. J., Aulanier, G., Title, A. M., Pariat, E., & Delannée, C. 2011, *ApJ*, 738, 167
- Shibata, K., & Magara, T. 2011, *Living Reviews in Solar Physics*, 8, 6
- Shine, R. A., Simon, G. W., & Hurlburt, N. E. 2000, *Sol. Phys.*, 193, 313
- Simon, G. W., Title, A. M., & Weiss, N. O. 2001, *ApJ*, 561, 427
- Taylor, G. I. 1938, *Proceedings of the Royal Society of London. Series A - Mathematical and Physical Sciences*, 164, 476

Uritsky, V. M., & Davila, J. M. 2012, ApJ, 748, 60

Uritsky, V. M., Davila, J. M., Ofman, L., & Coyner, A. J. 2013, Astrophysical J., 769, 62

Vemareddy, P., Ambastha, A., Maurya, R. A., & Chae, J. 2012, ApJ, 761, 86

Wang, S., Liu, C., Liu, R., et al. 2012, ApJ, 745, L17